nature electronics

Article

https://doi.org/10.1038/s41928-026-01660-x

Identification of the mode, polarization, wavelength and intensity of light using a one-pixel device on an optical fibre tip

Received: 28 August 2025

Accepted: 15 May 2026

Published online: 16 June 2026

Check for updates

Yifeng Xiong[1,2,9], Shaochen Fang[1,9], Yining Xu[1,9], Yu Lei[3], Lingyi Ao[1], Liuwei Zhan[1], Zixuan Ding[1], Hengtian Zhu[1], Maojie Chen[1], Zeya Li[1,4], Wencai Ren[5], Jinhui Chen[6], Ye Chen[7], Yan-qing Lu[1] ✉, Hongtao Yuan[1,8] ✉ & Fei Xu[1,2] ✉

The in situ monitoring of different parameters of light is important for the development of high-capacity information technology. However, the number of light states increases exponentially as parameters are added, and conventional detection systems must split light signals into numerous channels and photodetectors using bulky optics. Here we report a one-pixel device that is integrated on an optical fibre tip and can simultaneously resolve the mode, polarization, wavelength and intensity of light. The device, which can generate spatially dependent responses, is based on twisted, dichroic layers of two-dimensional black phosphorus and black arsenic–phosphorus, as well as ring-grating-like electrodes. The device generates six distinct photoresponses and we use it to achieve four-dimensional light detection with one-shot measurements, creating a large recognizable input-state space of around 10^4. We also show that the approach can be used for multidimensional image encryption communication.

The characterization of the intrinsic parameters of light—as derived from Maxwell's wave equations—is essential for the development of optical sensing[1,2], imaging[3,4], communication[5,6] and security encryption[7,8]. Guided waves in optical fibres carry, for example, a range of different information—including mode field, polarization, wavelength and intensity—that enhances the data-carrying capacity of a single fibre by orders of magnitude[9,10]. However, each additional parameter can lead to an exponential increase in the light state number, creating challenges for fibre demultiplexing systems that must split the light signal into numerous channels and photodetectors using bulky optics[11–13]. These ex situ detection strategies lead to high energy consumption, scanning-induced time delay, and additional noise and crosstalk during light propagation[14].

Despite attempts to design compact photodetectors capable of capturing light information beyond intensity—such as light field[15,16], polarization[17–23] or wavelength[24–31]—resolving these individual dimensions often requires different strategies. This makes integration and simultaneous processing challenging. Recent reports on joint polarization–wavelength–intensity detection using electrical scanning methods[1], as well as complementary-metal–oxide–semiconductor-based strategies[3,32], are also limited by detection speed and device compactness. This makes them unsuitable for the fast, in situ detection of different light parameters required for optical fibre sensing and communication.

In this Article, we report a device that is integrated on an optical fibre tip and can identify four-dimensional (4D) light parameters: mode

[1]National Laboratory of Solid State Microstructures, College of Engineering and Applied Sciences, and Collaborative Innovation Center of Advanced Microstructures, Nanjing University, Nanjing, China. [2]Shenzhen Research Institute of Nanjing University, Shenzhen, China. [3]School of Microelectronics and Data Science, Anhui University of Technology, Maanshan, China. [4]Quantum Science Center of Guangdong-Hong Kong-Macao Greater Bay Area, Shenzhen, China. [5]Shenyang National Laboratory for Materials Science, Institute of Metal Research, Chinese Academy of Sciences, Shenyang, China. [6]Institute of Electromagnetics and Acoustics, Xiamen University, Xiamen, China. [7]College of Physics, MIIT Key Laboratory of Aerospace Information Materials and Physics, Nanjing University of Aeronautics and Astronautics, Nanjing, China. [8]Jiangsu Key Laboratory of Artificial Functional Materials, Nanjing, China. [9]These authors contributed equally: Yifeng Xiong, Shaochen Fang, Yining Xu. ✉e-mail: yqlu@nju.edu.cn; htyuan@nju.edu.cn; feixu@nju.edu.cn

https://doi.org/10.1038/s41928-026-01660-x

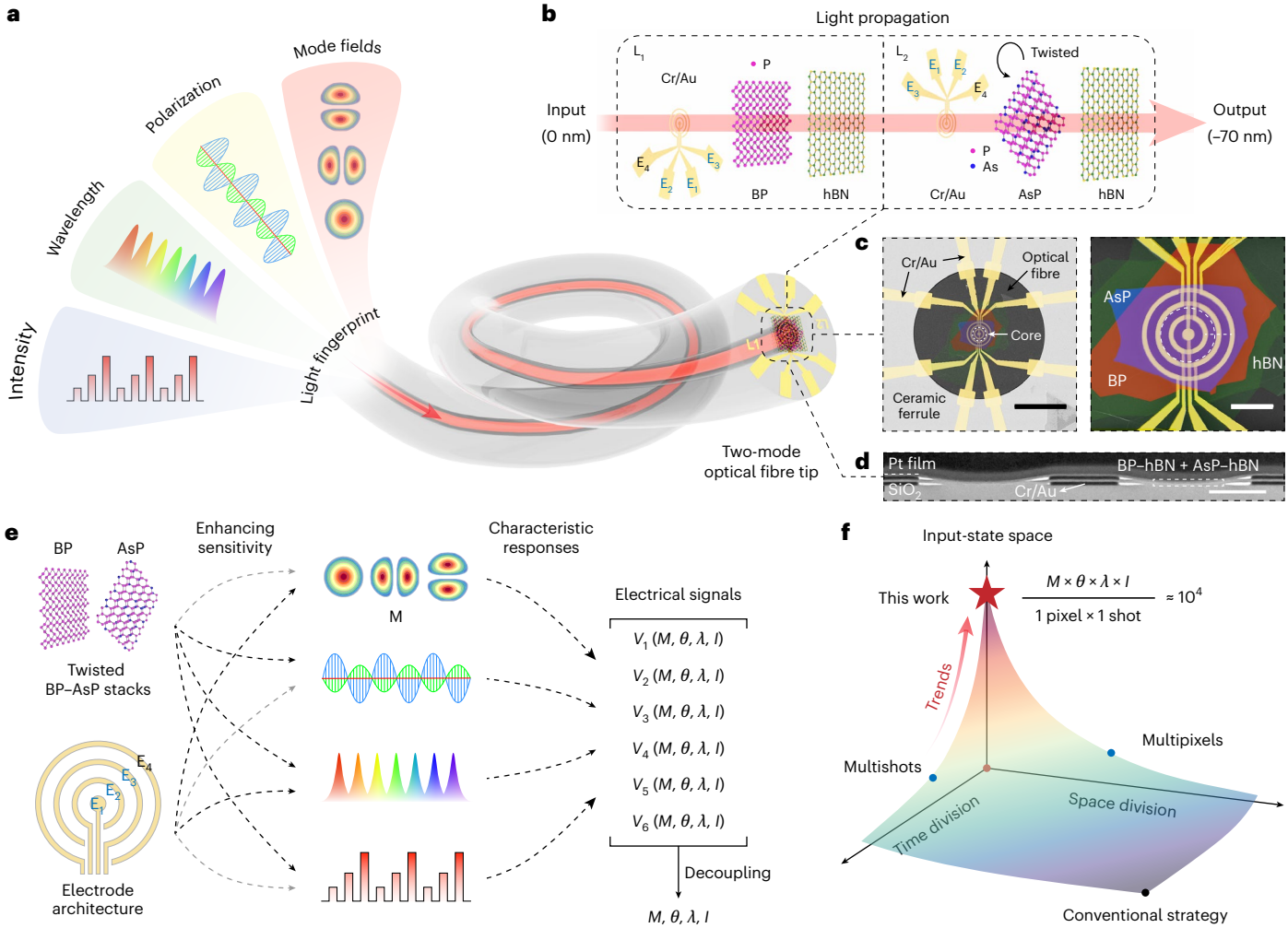

Fig. 1 | Fibre-integrated device for multidimensional light identification. **a**, Schematic of the device capable of analysing multiple light parameters. **b**, Two functional layers based on BP and AsP are twistedly stacked on an optical fibre endface, along light propagation. **c**, Pseudo-colour scanning electron microscopy images of the device. The left image shows the fibre device fixed in a ceramic ferrule. Scale bar, 50 µm. The right image is an enlarged view that highlights the stacked electrode architecture and functional materials. Scale bar, 10 µm. The white dashed circles represent the fibre core area. **d**, Cross-sectional transmission electron microscopy image of the device (along the white dashed line in **c**). Scale bar, 1 µm. The platinum (Pt) film is used to protect the sample during transmission electron microscopy fabrication. **e**, Sensitivities of 4D light parameters are enhanced by twisted BP–AsP stacks and electrode architecture, which lead to characteristic responses in terms of electrical signals for precise 4D light parameter decoupling. **f**, Our one-pixel device achieves 4D light parameter detection with numerous light states via a fast one-shot measurement, achieving high input-state space.

field (M), polarization (θ), wavelength (λ) and intensity (I). The device combines twisted dichroic materials with a wavelength scale, grating like multielectrode architecture, providing six distinct photoresponses via their combined interaction. In contrast to multipixel or multishot strategies (Fig. 1f), our approach achieves the fast in situ sensing of transmitted 4D light information using a one-pixel device (an active footprint of ~70-nm thickness and ~12-µm radius) with a one-shot measurement (~100-kHz detection speed; Supplementary Fig. 21). Due to distinct response differences in the light states, our device exhibits the high-precision recognition of 4D light parameters with minimal errors, achieving a large recognizable discrete input-state space of about 10^4 to handle large amounts of light information. We also show that our device can be used for high-dimensional image encryption communication.

Device architecture

The key to the identification of different light parameters lies in enhancing the sensitivity of the device to all relevant light parameters and effectively distinguishing these intricately coupled parameters through their characteristic responses. The device structure (Fig. 1a) consists of two multiport layers stacked on the endface of a two-mode fibre (Fig. 1b). Each layer contains three pairs of concentric ring electrodes covered by a thin film of black phosphorus (BP) or black arsenic–phosphorus (AsP) as the photoactive material, and a hexagonal boron nitride (hBN) nanoflake for insulation and encapsulation, which can be clearly identified in the scanning electron microscopy images (Fig. 1c) and transmission electron microscopy images (Fig. 1d and Supplementary Fig. 1) of the device. In the two layers, the outer-ring electrodes (E_4), serving as common ground electrodes, and the inner ring electrodes (E_1–E_3) together form a total of six detection ports (1–6), with Ports 1–3 located in the BP layer and Ports 4–6 located in the AsP layer. As shown in Fig. 1e, our design concept for 4D light parameter identification is as follows. First, the geometrical electrode architecture enhances sensitivity to fibre modes by inducing asymmetrical photoexciton generation under non-uniform mode fields. Its ring-grating-like structure drives diffraction-mediated, wavelength-dependent redistribution of light-field energy (Supplementary Section 2.3), yielding distinct self-driven photoresponses at spatially separated electrode pairs. Second, the BP and AsP layers, with differentiated chromatic dispersion and optoelectronic properties, provide complementary wavelength and intensity responses. These layers are twisted in crystal

orientations to generate complementary polarization-dependent photoresponses with specific phase shifts[18,23]. This three-dimensional structural and material design enables our miniaturized device to generate a set of differentiated photovoltage signals at six ports, each with multidimensional characteristic photoresponses $V_n(M,\theta,\lambda,I)$, where n is the number of detection ports, from a one-shot measurement, allowing for the efficient distinguishment of 4D light parameters through a simplified data processing technique.

To evaluate the multidimensional photosensing performance of the device, we built an experimental setup that allows the stepwise modulation of input light parameters and synchronous signal acquisition (Supplementary Fig. 19). In the experimental sequence, the wavelength (λ) is tuned via a tunable optical filter, the polarization angle (θ) is adjusted using a half-wave plate, the intensity (I) is regulated using a variable optical attenuator and the mode field (M) is defined through three optical switches, resulting in seven possible mode combinations. Under this controlled modulation scheme, all individual modes share essentially identical values of λ, θ and I, and the polarization phase retardation introduced by the photonic lantern remains constant across modes. Consequently, each input light state is uniquely defined by the tuple (M,θ,λ,I). On illumination, the device outputs six characteristic photovoltage channels, which are acquired quasi-simultaneously using a multichannel data acquisition card featuring high-speed channel switching and excellent interchannel isolation.

For mode-field sensing, we exploit the strongly non-uniform illumination of fibre modes. Figure 2a shows the electric-field distributions of the Gaussian-like LP_{01} and saddle-like LP_{11} modes along the two-mode fibre core, with the corresponding mode-adapted electrode layout clearly illustrated in Fig. 2b. This asymmetry in illumination on the photoactive materials drives unequal photocarrier injection into electrode pairs, leading to self-driven photoresponses (Fig. 2c). As a result, each fibre mode's distinct light-field distribution generates mode-specific self-driven responses in the structured electrodes (Fig. 2d).

For intensity sensing, the BP and AsP layers show distinct response curves (Fig. 2d), arising from differences in the weighting coefficients of their hybrid photogeneration mechanisms (Supplementary Fig. 14). Meanwhile, owing to illumination energy differences across electrode positions, each electrode pair exhibits distinct weighting coefficients and V_n–I response curves, enabling the accurate recognition of the intensity of each mode state.

For polarization sensing, the anisotropic BP and AsP layers exhibit strong dependence on the polarization state of the incident light. The polarization angle θ of the input light is tuned by rotating a half-wave plate, and the corresponding polarized photoresponses are mapped with respect to intensity and mode states (Fig. 2e). In each material layer, the photoresponses show distinct θ-dependent variations for different modes, arising from the intrinsic polarization differences preset among the modes (Fig. 2b). Owing to their twisted crystal orientations, BP and AsP produce V_n–θ curves with clear phase shifts under specific mode states, establishing a one-to-one V_n–θ relationship[18,23]. Under arbitrary mode combinations (Fig. 2f), the detection ports produce distinct intensity- and polarization-encoded photoresponses, with simultaneous multimode excitation causing response superposition, phase-angle shifts in V_n–θ curves and decreased polarization ratios.

For wavelength sensing, wavelength-dependent light-field localization at different electrode edges (Fig. 2g,h), where self-driven photogeneration predominantly occurs (Fig. 2c), produces varying responses across multiple detection ports[33]. The electrode structure, resembling a ring grating, induces the in-material-layer interference of diffraction waves, driving local field redistributions across electrode pairs and yielding distinct responses. Meanwhile, this interference modulated by the surrounding refractive index, together with the complex refractive index contrast between BP and AsP arising from their compositional variations[34–36], generates complementary wavelength-dependent responses in the two material layers (Fig. 2i). These combined effects of material dispersion and electrode geometry uniquely encode discrete-wavelength points in the six-port photoresponse set, allowing the device to operate effectively as an enhanced wavelength meter. In particular, fibre dispersion alters the effective refractive indices of different modes, modifying the light-field distribution at the fibre facet. As a result, wavelength responses in the fibre may deviate from ideal simulations; however, our light-field-based detection approach can effectively compensate for these discrepancies, provided the wavelength is precisely calibrated.

Decoupling with characteristic responses

Multidimensional light incidence leads to an intricate coupling of parameters in each signal output, thereby requiring dedicated decoupling processes. We first evaluate the device's capability to recognize discrete 4D light states. This is achieved by constructing a discrete precalibration database, in which the measured photoresponses of 4D light parameters are mapped as θ–I curved surfaces across different λ and M states (Fig. 3a). The response specificity to different multidimensional states is characterized by photovoltage differences (D) across multiple ports[3]. In total, we distinguish 7 mode fields, 7 wavelengths, 19 polarization states and 10 intensities, yielding 9,310 ($7\times7\times19\times10$) distinct input states. The difference matrix of these 4D states is shown in Supplementary Fig. 32, where the response differences are found to exceed device noise fluctuations, indicating that these states can, in principle, be reliably distinguished. During operation, the six-port photoresponses are compared with the precalibration database via root mean square error (RMSE)-based 1-nearest-neighbour (1-NN) search. The database entry yielding the minimum RMSE—corresponding to the closest match—is designated as the output state (Methods). For example, Fig. 3b shows that the incident LP_{11y} mode is correctly resolved, exhibiting the lowest RMSE among all mode states. Figure 3c further displays the RMSE distribution for correctly and incorrectly identified states, where the correct results exhibit notable lower RMSE levels, demonstrating the high recognition accuracy of the decoupling process. Building on this, the cross matrices in Supplementary Fig. 30 illustrate that the device successfully decouples 9,310 light states with an accuracy exceeding 99%, underscoring its robust performance. In addition, to assess the contribution and potential redundancy of the six ports, we performed tensor decomposition analysis of the measured response signals, which reveals that the device effectively extracts a 4D information space from the six-port read-out, indicating partial redundancy (Supplementary Section 6.6). By evaluating 4D light identification using different combinations of ports, we find that the four ports located near the device centre already achieve identification accuracies exceeding 97%, whereas the outer-ring ports mainly provide redundant information that enhances robustness and noise tolerance.

Apart from the discrete nature of mode states, polarization, wavelength and intensity vary continuously, requiring an accurate prediction between calibration points. To address this, we establish databases precisely calibrated along a single light dimension (polarization, wavelength or intensity) and refine them using a typical spline interpolation method. The same RMSE-based decoupling procedure is then applied to identify the state closest to the refined calibration database, which is taken as the output. In particular, all testing data are entirely independent of the precalibrated database, including both states identical to those in calibration and completely uncalibrated states. Recognition accuracy is quantified by the average offset (ΔX) and average standard deviation (σX), where lower values signify higher accuracy (Methods provides full definitions). For linear polarization recognition (Fig. 3d), accuracies reach $\Delta\theta_c$ = ~0.14° and $\sigma\theta_c$ = ~0.58° for calibrated states (indicated using subscript 'c'), and $\Delta\theta_u$ = ~0.34° and $\sigma\theta_u$ = ~1.49° for predicted unknown states (indicated using subscript 'u'), under a 4° precalibration step within the 0°–90° range. For single-peak wavelength recognition (Fig. 3e), accuracies reach $\Delta\lambda_c$ = ~0.016 nm, $\sigma\lambda_c$ = ~0.04 nm for calibrated states, and $\Delta\lambda_u$ = ~0.12 nm, $\sigma\lambda_u$ = ~0.25 nm

https://doi.org/10.1038/s41928-026-01660-x

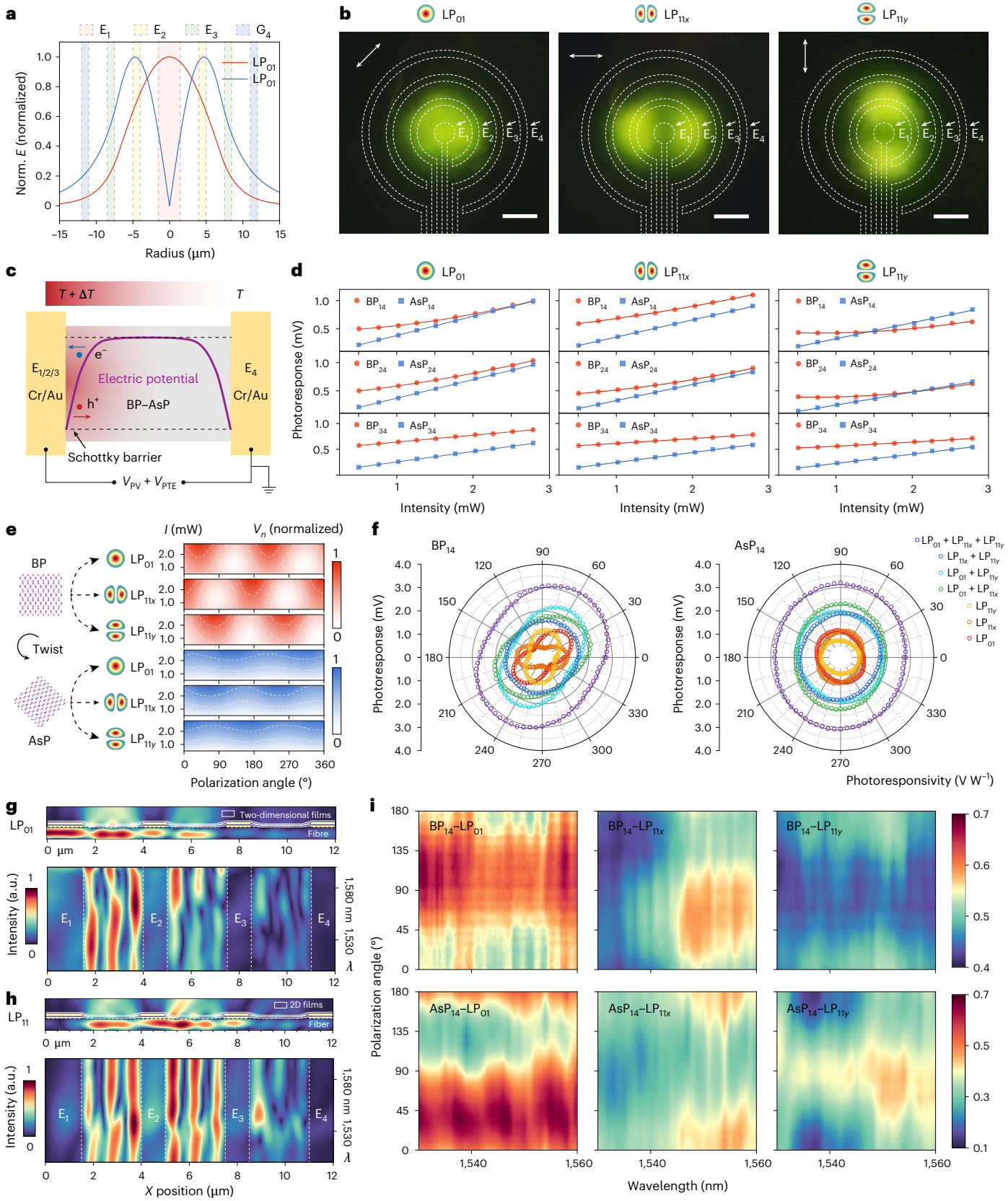

Fig. 2 | Multidimensional sensitivity of the device. a, Simulated electric-field profiles of two modes in a two-mode fibre, overlaid with the electrode distributions. **b**, Upconverted images of mode fields under different polarization states, with the dashed outlines indicating electrode geometry. Scale bar, 5 μm. **c**, Asymmetric illumination induces non-uniform temperature gradients, electric potential and photoexciton separation in the metal–semiconductor–metal region. **d**, Photoresponse of each port in BP and AsP layers versus intensity, under different mode fields. **e**, Twisted crystals produce polarization-dependent photoresponses in BP (top three panels) and AsP (bottom three panels), under different modes. **f**, Polar plots of the photoresponse of BP and AsP layers as functions of polarization angles, under different mode combinations. **g**,**h**, Simulated cross-sectional and wavelength-dependent light-field distributions under LP_{01} (**g**) and LP_{11} (**h**) modes. **i**, Photoresponsivity of BP and AsP layers related to the wavelength, polarization and mode fields.

https://doi.org/10.1038/s41928-026-01660-x

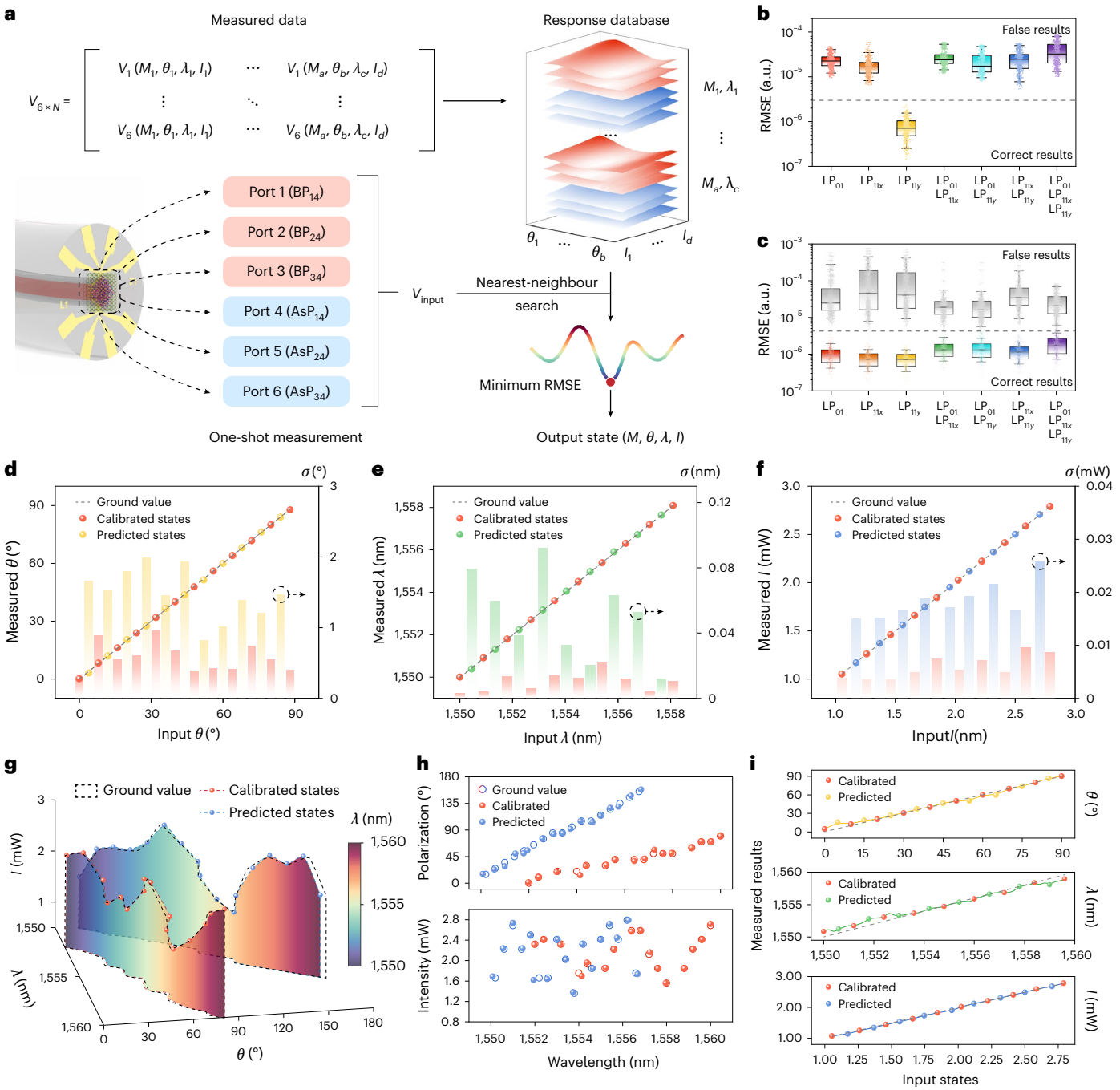

Fig. 3 | Multidimensional decoupling process. a, Schematic of the algorithm for resolving 4D light parameters. **b**, Statistical RMSE values of all mode states when the LP_{11y} mode is illuminated. The sample size is $n = 570$ independent data points. **c**, Correctly executed decoupling results of different mode states with low RMSE values, compared with incorrect results (grey boxes) associated with high RMSE values. The sample size is $n = 570$ correctly identified data points and $n = 3{,}420$ incorrectly identified data points. The box plots in **b** and **c** indicate the median (middle line), 25th and 75th percentile (box), and 5th and 95th percentile (whiskers), with individual data points overlaid. **d**–**f**, Decoupling results of individual light dimensions, including polarization (**d**), wavelength (**e**) and intensity (**f**). The hollow circles indicate the reference values, the red points are reconstructed results of calibrated states, and other coloured points are prediction results of unknown states. The histograms refer to statistical mean standard deviation values under different states. **g**, Decoupling of a series of polarization–wavelength–intensity states: the black dashed line indicates the ground-truth values; the red and blue dashed lines represent the decoupling of calibrated states and unknown states, respectively. **h**, Decoupling results from **g** are projected onto the λ–θ and λ–I planes for better clarity and analysis. **i**, Decoupling results of each dimension under multidimensional light incidence in **g**, including polarization (top), wavelength (middle) and intensity (bottom).

for predicted unknown states, with a 0.1-nm precalibration step over the range of 1,550–1,558 nm. For intensity recognition (Fig. 3f), accuracies reach $\Delta I_c = \sim 1.68 \times 10^{-4}$ mW and $\sigma I_c = \sim 5.90 \times 10^{-3}$ mW for calibrated states, and $\Delta I_u = \sim 1.12 \times 10^{-3}$ mW and $\sigma I_u = \sim 1.85 \times 10^{-2}$ mW for predicted unknown states, with a 0.2-mW precalibration step over the range of 1.0–2.8 mW. Owing to the complementary and distinct responses of the six detection ports, the detection accuracies achieved for individual light dimensions are comparable with those of state-of-the-art single-purpose compact devices (Supplementary Table 1). Compared with the calibrated states, where minimal errors mainly reflect noise fluctuations, the higher errors in unknown states reasonably highlight the device's predictive capability beyond calibration.

https://doi.org/10.1038/s41928-026-01660-x

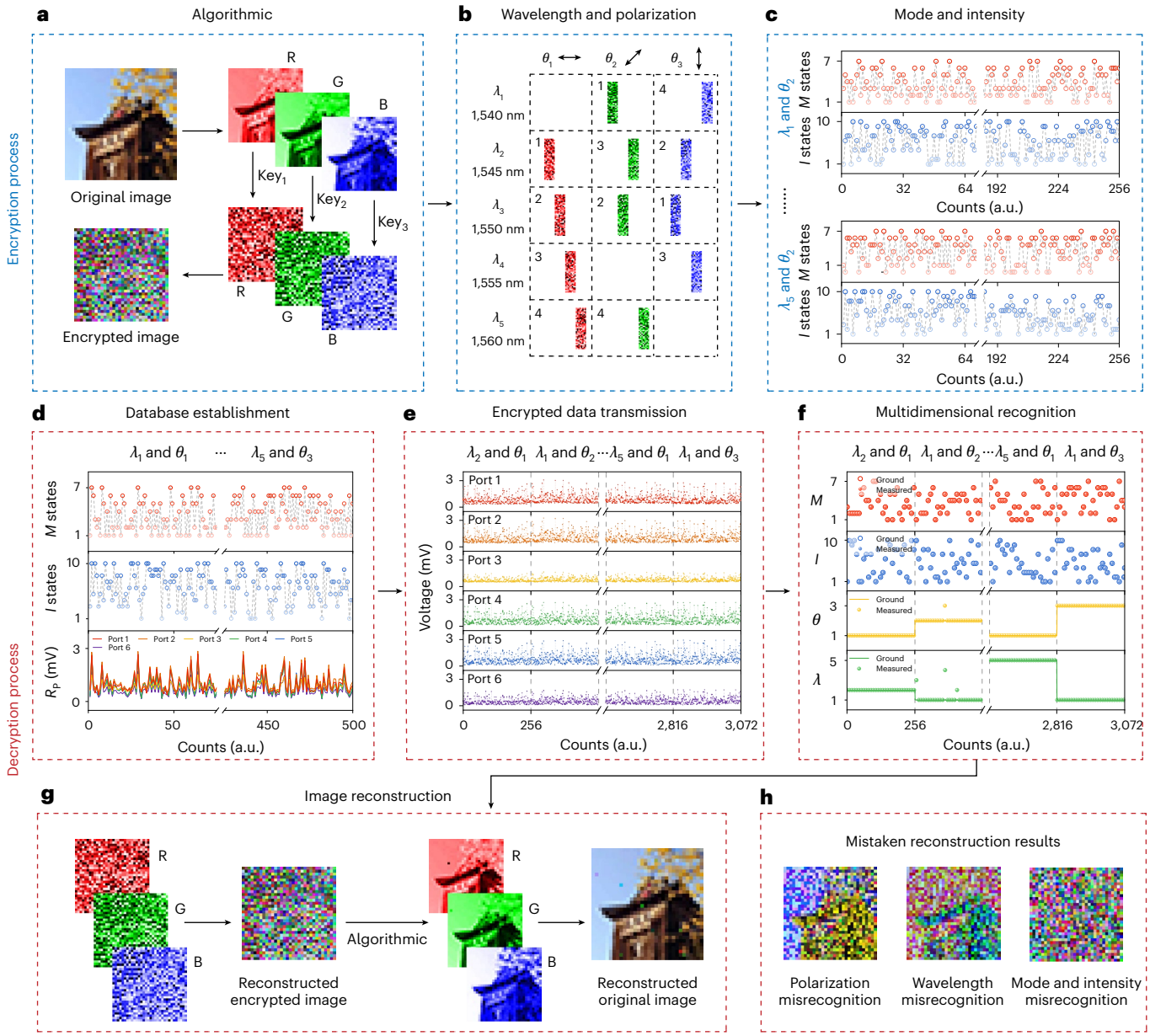

Fig. 4 | Multidimensional image encryption/decryption process. a, Schematic of the encryption process. **b**, Polarization and wavelength modulation on segments of ciphertext. The sequence of segments indicates sequential transmission. Polarization states (θ_{1-3}) refer to RGB channels and wavelengths (λ_{1-5}) refer to the hidden keys. **c**, Ciphertext loaded on mode and intensity states, from the first segment (top) to the last segment (bottom). **d**, Database-establishing process. Incident light carrying mode (top) and intensity (middle) states are calibrated using the photovoltage responses (bottom) of the device. **e**, Photovoltage responses of six ports in BP and AsP layers with encrypted light states. **f**, 4D light parameter recognition results of the received data. Sequential segments of ciphertext carrying different wavelengths and polarizations are shown from left to right. **g**, Image reconstruction process using received ciphertext and keys. **h**, Simulated mistaken reconstructed results when the device lacks fully recognition ability to 4D light parameters.

Next, we assess the device's capability to identify unknown multidimensional light incidence using six feature-rich photoresponses from a single measurement. By leveraging high-dimensional precalibration and three-dimensional interpolation, we construct a precise, refined dataset for accurate state reconstruction. Using the same decoupling procedure, both calibrated and previously uncalibrated light states with varying polarization, wavelength and intensity are reconstructed with high accuracy (Fig. 3g, h). Statistical analysis across all dimensions yields comprehensive accuracies of $\Delta\theta_c = 1.15°$, $\Delta\lambda_c = 0.33$ nm and $\Delta I_c = 1.33 \times 10^{-3}$ mW for calibrated states, and $\Delta\theta_u = 3.54°$, $\Delta\lambda_u = 0.46$ nm and $\Delta I_u = 1.53 \times 10^{-3}$ mW for predicted unknown states (Fig. 3i). Unlike conventional methods that rely on extensive multishot or multipixel sampling, our approach resolves high-dimensional light parameters from a single shot using a simple algorithm, drastically reducing data requirements and enabling ultrafast processing (approximately microseconds on a personal computer, with further acceleration via parallelization; Supplementary Section 6.5).

Multidimensional image encryption communication

As a proof of concept, we demonstrate an image encryption communication process, where image data are encrypted using 4D light parameters for transmission, subsequently decrypted by our device, and finally reconstructed through an algorithm. Figure 4a illustrates the encryption scheme, in which a 6-bit original image is divided into three images in RGB channels using three polarization states θ_1, θ_2 and θ_3.

In each RGB channel, the image data are encrypted using logistic chaotic systems[37], and the decisive keys for logistic mapping (Methods) are encoded into wavelength states that are sequentially loaded onto pixel segments (Fig. 4b, rows) and are distinct between RGB channels (Fig. 4b, columns). After conversion into ciphertext, the image data are encoded into mode and intensity states (64 different combinations in total), and synchronously carry both colour and encryption keys during the transmission (Fig. 4c). In particular, our demonstration provides key space size over 10^8 (Supplementary Section 7.2) for security against attacks[38].

The decryption process requires a precise identification of 4D light parameters and algorithmic reconstruction of the original image. The device is first calibrated by establishing a database with random mode and intensity states under varying wavelengths and polarization conditions (Fig. 4d). Then, the sequentially encrypted information is transmitted in the fibre and converted into photovoltage signals by the six ports of the device (Fig. 4e). These responses are recognized as 4D light states (Fig. 4f), and the data segments are rearranged into RGB channels according to different polarizations, providing three different wavelength sequences. Finally, the ciphertext is filled into RGB layers and decrypted using hidden keys acquired from the wavelength sequence in each layer, achieving a structural similarity index measure of 0.9917 between the reconstructed image and the original image (Fig. 4g). It is worth noting that the reconstructed image is damaged if the device is missing or imprecise in a certain light dimension. We simulate three typical mistaken reconstruction results (Fig. 4h) to highlight the importance of multidimensional light detection technology in improving information capacity and security.

Conclusions

We have reported the one-shot detection of 4D light parameters using a one-pixel device on a fibre tip. The device architecture enhances the photosensitivity to all light dimensions and generates characteristic photoresponses for precise light parameter identification, eliminating the need for external photodetector arrays, filter arrays, bulky polarization/dispersive components, collimators and focusing lenses. Our device can support around ~10^4 separate light states (Supplementary Fig. 32), and this state space could be further expanded by refining the discretization of each individual light dimension.

By using the distinct polarization and light-field distributions of linear polarized modes, our device can recognize multiple modes in high-dimensional mode spaces, such as those supported in a four-mode fibre (Supplementary Section 2.5). However, extending this approach to multimode fibres with additional modes is challenging, as stable mode-dependent distinguishable responses are difficult to maintain in this situation. The symmetry breaking induced by the metal–semiconductor Schottky junction[18] allows the device to detect circular and elliptical polarizations and, in principle, support full-Stokes identification for polarization-only tasks (Supplementary Section 5.4). However, signal overlap and calibration difficulty in the presence of simultaneous 4D variations make full-Stokes reconstruction a challenge in the current multidimensional setting.

Our device operates in a wavelength-meter mode and does not aim at full spectral reconstruction such as broadband chemical sensing or wavelength division multiplexing, because of the limited encoding dimensionality available in a single-shot measurement. This discrete-wavelength operation is well suited to applications such as fibre-optic monitoring, wavelength locking and optical encryption, where the rapid and accurate identification of the incident centre wavelength is essential. Furthermore, the BP–AsP heterostructure supports phototransistor-like operation, and thus, electrically induced spectral modulation could be used to enrich the encoding space and support broadband spectral reconstruction in future implementations (Supplementary Section 5.5).

Methods

Device fabrication

The sequential fabrication processes of the device are shown below. (1) Preparation and cleaning: the commercially available silica two-mode optical fibre (FM2010-B, YOFC) is fixed with a ceramic ferrule (125-μm inner diameter, 2.5-mm outer diameter) and ground to obtain a flat fibre–ferrule endface, followed by a thorough cleaning process. (2) L_1 electrode fabrication: we proceed to the optimized electron-beam lithography (Mira, Tescan) to create the desired patterns, using electron-beam evaporation (PVD75 Proline EB, Kurt J. Lesker) to deposit metal electrodes (10 nm of Cr and 40 nm of Au). (3) Material preparation and transfer: mechanical exfoliation is used to prepare BP and hBN films (SixCarbon Technology Shenzhen) on polydimethylsiloxane, which are then transferred to polycarbonate films. The prepared BP and hBN films on polycarbonate polymer films are successively transferred to the optical fibre endface using an optimized dry transfer method. (4) Subsequent layer fabrication: following similar fabrication steps, L_2 electrodes, AsP layer and hBN layer are fabricated step by step. Note that the fabrication, preservation, transportation and measurements of the device are conducted in an air-free environment (vacuum or N_2 atmosphere) to minimize the degradation of BP and AsP as much as possible. The more detailed fabrication processes are shown in Supplementary Section 3.

Decoupling of 4D light parameters

When incident light illuminates the device, the photoresponse of the device can be obtained from the six ports and decoupled using the previously calibrated database in three steps. (1) Calculate the RMSE between the measured data and the database entries calibrated with specific mode and wavelength conditions. (2) Record the intensity and polarization states corresponding to the minimum RMSE value under different conditions. (3) Identify the lowest RMSE among all conditions to confirm the mode and wavelength state, together with the corresponding intensity and polarization state, to serve as the 4D light parameters of the incident light. Considering the size of database needed and the recognition error, our method based on RMSE calculation has an advantage over other alternative approaches, including classification/regression algorithms and even artificial neural networks. The details of the RMSE calculation can be expressed as $\mathrm{RMSE} = \sqrt{\sum_{n=1}^{6}(V_{\mathrm{light}} - V_{\mathrm{cali}})^2/6}$, where V_{light} and V_{cali} refer to the response of incident light and calibrated states and n is the index of the six ports. RMSEs represents the 'distance' between the unknown incident light and the calibrated states, located by the responses of the six ports.

Analysis of the recognition results

We use the average offset (ΔX) and the average standard deviation (σX) of different input states to characterize the recognition accuracy of device. For specific light dimension X, the average offset is calculated by $\Delta X = \frac{1}{N}(\sum_{i=1}^{N}|X_i - X_0|)$, where X_i and X_0 refer to the measured and reference value, respectively, and N is the total number of sample counts. The average standard deviation is $\sigma X = \frac{1}{B}(\sum_{b=1}^{B}\sqrt{\sum_{a=1}^{A}(X_a - \bar{X})^2/A})$, where X_a and $\bar{X}$ refer to individual and average decoupled value, A is the number of measurements of each input state and B is the total amount of states ($N = \mathrm{A} \times \mathrm{B}$). ΔX indicates the probable deviation in measurements and εX reflects the stability across multiple measurements, where low values of both signify minimal decoupling error and high repeatability. Further details of the deviation analysis are provided in Supplementary Section 6.2.

Image encryption communication

In the experiment, we choose a 32 × 32 RGB image to show the advantages of 4D light parameter detection. Seven mode fields and ten intensities are used to convey the 6-bit depth information of a single pixel in different RGB channels. 0°, 45° and 90° polarization states represent the R, G and B channels, respectively, whereas distinct wavelengths

sequentially loaded onto RGB channels carry different keys for encryption and decryption (Supplementary Fig. 39). We provide the polarization and wavelength states according to the encryption scheme, where the θ and λ show the transmission sequence in different polarization states (RGB channels), for example, the λ sequence '4213' indicates the wavelength modulation in θ_3 (90°) channel is (λ_3, λ_2, λ_4, λ_1). Supplementary Fig. 39c illustrates the mapping relationship between wavelength and r values used for the logistic random sequence encryption, and the (λ_3, λ_2, λ_4, λ_1) sequence mentioned above corresponds to the key value r = 3.95 3 7 1, where the four digits after 3.9 are mapped by the λ index. In our demonstration, the hidden keys carried by wavelength information are Rr = 3.93579, Gr = 3.91539 and Br = 3.95371, thereby achieving the image encrypted transmission.

Regarding the details of image encryption, different r values are used for generating random sequences, which enable different encryptions of the original image. Using a specific r and an initial value $X(0) = 0.5$, the random sequence can be expressed as $X_{i+1} = r \times X_i \times (1 - X_i)$. The generated sequence X is scaled to the range of 0 to 63 as X', corresponding to the 6-bit information. A bitwise XOR operation is then performed between X' and the original image (Supplementary Fig. 40) to produce the encrypted image. The encrypted image is transmitted as ciphertext and the decrypted image can be obtained by performing a bitwise XOR operation with X' again (Fig. 4g). Additionally, the encrypted depth information tends to be more randomly distributed compared with the original depth, which is compatible with the random calibration mentioned in Fig. 4d.

Data availability

The source data for this study are available via Figshare at https://doi.org/10.6084/m9.figshare.29412878 (ref. 39). Other data that support the findings of this study are available from the corresponding authors upon request. Source data are provided with this paper.

Code availability

The codes that support the findings of this study are available from the corresponding authors upon reasonable request.

References

1. Ma, C. et al. Intelligent infrared sensing enabled by tunable moire quantum geometry. *Nature* **604**, 266–272 (2022).
2. Yuan, S. et al. Geometric deep optical sensing. *Science* **379**, eade1220 (2023).
3. Fan, Y. et al. Dispersion-assisted high-dimensional photodetector. *Nature* **630**, 77–83 (2024).
4. Song, I. et al. Helical polymers for dissymmetric circularly polarized light imaging. *Nature* **617**, 92–99 (2023).
5. Richardson, D. J., Fini, J. M. & Nelson, L. E. Space-division multiplexing in optical fibres. *Nat. Photon.* **7**, 354–362 (2013).
6. Winzer, P. J. Making spatial multiplexing a reality. *Nat. Photon.* **8**, 345–348 (2014).
7. Fang, X., Ren, H. & Gu, M. Orbital angular momentum holography for high-security encryption. *Nat. Photon.* **14**, 102–108 (2019).
8. Ouyang, X. et al. Synthetic helical dichroism for six-dimensional optical orbital angular momentum multiplexing. *Nat. Photon.* **15**, 901–907 (2021).
9. van Uden, R. G. H. et al. Ultra-high-density spatial division multiplexing with a few-mode multicore fibre. *Nat. Photon.* **8**, 865–870 (2014).
10. Liu, J. et al. 1-Pbps orbital angular momentum fibre-optic transmission. *Light: Sci. Appl.* **11**, 202 (2022).
11. Li, K. et al. Fiber-chip-fiber mode/polarization/wavelength transmission and processing with few-mode fiber, (de) multiplexing SiO_2 chip and ROADM Si chip. *Laser Photon. Rev.* **18**, 2300489 (2024).
12. Gregg, P. et al. Enhanced spin orbit interaction of light in highly confining optical fibers for mode division multiplexing. *Nat. Commun.* **10**, 4707 (2019).
13. Rademacher, G. et al. Peta-bit-per-second optical communications system using a standard cladding diameter 15-mode fiber. *Nat. Commun.* **12**, 4238 (2021).
14. Lu, K. et al. Empowering high-dimensional optical fiber communications with integrated photonic processors. *Nat. Commun.* **15**, 3515 (2024).
15. Ji, Z. et al. Photocurrent detection of the orbital angular momentum of light. *Science* **368**, 763–767 (2020).
16. Lien, M. B. et al. Ranging and light field imaging with transparent photodetectors. *Nat. Photon.* **14**, 143–148 (2020).
17. Wei, J. et al. Zero-bias mid-infrared graphene photodetectors with bulk photoresponse and calibration-free polarization detection. *Nat. Commun.* **11**, 6404 (2020).
18. Xiong, Y. et al. Twisted black phosphorus-based van der Waals stacks for fiber-integrated polarimeters. *Sci. Adv.* **8**, eabo0375 (2022).
19. Dai, M. et al. On-chip mid-infrared photothermoelectric detectors for full-Stokes detection. *Nat. Commun.* **13**, 4560 (2022).
20. Dai, M. et al. Long-wave infrared photothermoelectric detectors with ultrahigh polarization sensitivity. *Nat. Commun.* **14**, 3421 (2023).
21. Wei, J., Xu, C., Dong, B., Qiu, C.-W. & Lee, C. Mid-infrared semimetal polarization detectors with configurable polarity transition. *Nat. Photon.* **15**, 614–621 (2021).
22. Wei, J. et al. Geometric filterless photodetectors for mid-infrared spin light. *Nat. Photon.* **17**, 171–178 (2022).
23. Wang, F. et al. Multidimensional detection enabled by twisted black arsenic-phosphorus homojunctions. *Nat. Nanotechnol.* **19**, 455–462 (2024).
24. Yoon, H. H. et al. Miniaturized spectrometers with a tunable van der Waals junction. *Science* **378**, 296–299 (2022).
25. Yang, Z., Albrow-Owen, T., Cai, W. & Hasan, T. Miniaturization of optical spectrometers. *Science* **371**, eabe0722 (2021).
26. Yang, Z. et al. Single-nanowire spectrometers. *Science* **365**, 1017–1020 (2019).
27. Grotevent, M. J. et al. Integrated photodetectors for compact Fourier-transform waveguide spectrometers. *Nat. Photon.* **17**, 59–64 (2023).
28. Yuan, S., Naveh, D., Watanabe, K., Taniguchi, T. & Xia, F. A wavelength-scale black phosphorus spectrometer. *Nat. Photon.* **15**, 601–607 (2021).
29. He, X. et al. A microsized optical spectrometer based on an organic photodetector with an electrically tunable spectral response. *Nat. Electron.* **7**, 694–704 (2024).
30. Bao, J. & Bawendi, M. G. A colloidal quantum dot spectrometer. *Nature* **523**, 67–70 (2015).
31. Du, X. et al. A microspectrometer with dual-signal spectral reconstruction. *Nat. Electron.* **7**, 984–990 (2024).
32. Zhu, S. et al. Harnessing disordered photonics via multi-task learning towards intelligent four-dimensional light field sensors. *PhotoniX* **4**, 26 (2023).
33. He, T. et al. On-chip optoelectronic logic gates operating in the telecom band. *Nat. Photon.* **18**, 60–67 (2023).
34. Yuan, H. et al. Polarization-sensitive broadband photodetector using a black phosphorus vertical p-n junction. *Nat. Nanotechnol.* **10**, 707–713 (2015).
35. Bullock, J. et al. Polarization-resolved black phosphorus/molybdenum disulfide mid-wave infrared photodiodes with high detectivity at room temperature. *Nat. Photon.* **12**, 601–607 (2018).
36. Biswas, S., Grajower, M. Y., Watanabe, K., Taniguchi, T. & Atwater, H. A. Broadband electro-optic polarization conversion with atomically thin black phosphorus. *Science* **374**, 448–453 (2021).

37. Wong, K.-W., Kwok, B. S.-H. & Yuen, C.-H. An efficient diffusion approach for chaos-based image encryption. *Chaos Solitons Fractals* **41**, 2652–2663 (2009).
38. Guan, Z.-H., Huang, F. & Guan, W. Chaos-based image encryption algorithm. *Phys. Lett. A* **346**, 153–157 (2005).
39. Xiong, Y. et al. Source data for 'Identification of the mode, polarization, wavelength and intensity of light using a one-pixel device on an optical fibre tip'. *Figshare* https://doi.org/10.6084/m9.figshare.29412878 (2026)

Acknowledgements

This work was supported by the National Key R&D Program of China under grant numbers 2021YFA1401103 (F.X.) and 2024YFA1408104 (H.Y.); the Natural Science Foundation of Jiangsu Province under grant numbers BK20243014 (F.X.), BK20230769 (Y. Xiong), BK20253012 (H.Y.), BK20233001 (H.Y.) and BK20243011 (H.Y.); the National Natural Science Foundation of China under grant numbers 61925502 (F.X.), 62135007 (F.X.), 62305153 (Y. Xiong), U24A6002 (H.Y.) and 92365203 (H.Y.); the Guangdong Basic and Applied Basic Research Foundation under grant numbers 2023B1515120011 (F.X.), 2025A1515012111 (Y. Xiong) and 2026A1515011759 (Z.L.); Fujian Provincial Natural Science Foundation of China under grant number 2023J06011 (J.C.); the Guangdong Provincial Quantum Science Strategic Initiative under grant number GDZX2501002 (Z.L.); the Shenzhen Municipal Funding Co-Construction Program Project under grant number SZZX2501001 (Z.L.); and Talent Project Scientific Research Foundation of Anhui University of Technology under grant number QD202378 (Y. Lei). We thank Q. Y. Shao, R. Z. Zhu and Z. Xu for help in the work.

Author contributions

F.X. conceived the project. Y. Xiong, S.F. and Z.D. performed the methodology construction and device design. Y. Xiong and Y. Xu prepared the samples. Y. Xiong, S.F., L.Z., M.C. and Y.C. constructed the experimental setups. Y. Xiong, S.F. and Y. Xu performed the measurements. Y. Xu, L.A. and Z.L. performed the material characterizations. W.R. contributed to the related materials. Y. Xiong, S.F., Y. Xu, Y.-q.L., H.Z., Y.C., J.C., Y. Lu, H.Y. and F.X. discussed and analysed the results. Y. Xiong, S.F., Y.-q.L., H.Z., Y.C., J.C., Y. Lu, H.Y. and F.X. wrote the paper. F.X. supervised the project.

Competing interests

The authors declare no competing interests.

Additional information

Supplementary information The online version contains supplementary material available at https://doi.org/10.1038/s41928-026-01660-x.

Correspondence and requests for materials should be addressed to Yan-qing Lu, Hongtao Yuan or Fei Xu.

Peer review information *Nature Electronics* thanks Wei Li, Fan Zhang and the other, anonymous, reviewer(s) for their contribution to the peer review of this work.